STP 1597, 2018 / available online at www.astm.org / doi: 10.1520/STP159720160076

Aditya P. Shivprasad,[1] Arthur T. Motta,[1] Aylin Kucuk,[2]
Suresh Yagnik,[2] and Zhonghou Cai[3]

Microbeam X-Ray Absorption Near-Edge Spectroscopy of Alloying Elements in the Oxide Layers of Irradiated Zircaloy-2

Citation

Shivprasad, A. P., Motta, A. T., Kucuk, A., Yagnik, S., and Cai, Z., "Microbeam X-Ray Absorption Near-Edge Spectroscopy of Alloying Elements in the Oxide Layers of Irradiated Zircaloy-2," *Zirconium in the Nuclear Industry: 18th International Symposium*, *ASTM STP1597*, R. J. Comstock and A. T. Motta, Eds., ASTM International, West Conshohocken, PA, 2018, pp. 524–554, http://dx.doi.org/10.1520/STP159720160076[4]

ABSTRACT

Hydrogen pickup of zirconium-based fuel cladding and structural materials during in-reactor corrosion can degrade fuel components because the ingress of hydrogen can lead to the formation of brittle hydrides. In the boiling water reactor (BWR) environment, Zircaloy-2 fuel cladding and structural components such as water rods and channels can experience accelerated hydrogen pickup, whereas Zircaloy-4 components exposed to similar conditions do not. Because the principal difference between the two alloys is that Zircaloy-2 contains nickel, accelerated hydrogen pickup has been hypothesized to result from the presence of nickel. However, an understanding of the mechanism by which this acceleration occurs is still lacking. We investigated the link between hydrogen pickup and the oxidation behavior of alloying elements when incorporated into the oxide layers formed on zirconium alloys when corroded in the reactor.

Manuscript received March 20, 2016; accepted for publication November 10, 2016.
[1]Pennsylvania State University, Dept. of Mechanical and Nuclear Engineering, University Park, PA 16802
A. S. http://orcid.org/0000-0001-8515-2756 A. M. http://orcid.org/0000-0001-5735-1491
[2]Electric Power Research Institute, Palo Alto, CA 94304
[3]Advanced Photon Source, Argonne National Laboratory, Argonne, IL 60439
[4]ASTM 18th International Symposium on *Zirconium in the Nuclear Industry* on May 15-19, 2016 in Hilton Head, SC.

Synchrotron radiation microbeam X-ray absorption near-edge spectroscopy (XANES) at the Advanced Photon Source was performed on carefully selected BWR-corroded Zircaloy-2 water rods at an assembly-averaged burnup ranging from 32.8 to 74.6 GWd/MTU to determine the oxidation states of alloying elements, such as iron and nickel, within the oxide layers as a function of distance from the oxide-metal interface at high burnup. Samples were chosen for comparison based on having similar oxide thicknesses, processing, elevation, reactors, and fluences but different hydrogen pickup fractions. Examinations of the oxide layers formed on these samples showed that (1) the oxidation states of these alloying elements changed with distance from the oxide-metal interface, (2) these elements exhibited delayed oxidation relative to the host zirconium, and (3) nickel in Zircaloy-2 remained metallic in the oxide layer at a longer distance from the oxide-metal interface than iron. An analysis of these results showed an apparent correlation between the delayed oxidation of nickel and higher hydrogen pickup of Zircaloy-2 at high burnup.

Keywords

Zircaloy-2, hydrogen pickup, XANES, alloying elements, high burnup, oxidation state

Introduction

During the initial development of nuclear fuel cladding for light-water reactors, the large variance in mechanical behavior seen in notched-bar impact testing of both out-of-pile and in-reactor–corroded Zircaloy-2 was attributed to a hydride phase that formed because of high hydrogen pickup [1,2]. Detailed corrosion testing of zirconium alloy coupons of various compositions showed that alloys with higher nickel content absorbed larger quantities of hydrogen. The removal of nickel altogether significantly reduced the percentage of hydrogen absorbed relative to the amount produced during the corrosion reaction, called the hydrogen pickup fraction (HPUF) [3–6]. The subsequent removal of nickel from Zircaloy-2 and optimization of alloying-element contents resulted in the development of Zircaloy-4. However, because Zircaloy-2 exhibited better corrosion resistance in steam environments, it became the industry standard for the boiling water reactor (BWR) fuel cladding [2,7,8]. Although the hydrogen pickup properties of Zircaloy-2 have been studied since its development, the role of nickel in promoting hydrogen pickup is not well understood.

HPUF has been used in the past as a measure of the tendency of a material to absorb hydrogen. It should be noted, however, that because of the complex phenomena involved, HPUF is not an inherent physical property of the material per se but the result of the interaction of material properties with the corrosion environment. In addition, because HPUF depends directly on the oxide layer thickness, a higher HPUF does not necessarily mean higher hydrogen content.

Early studies performed by Yeniscavich, Wolfe, and Lieberman [3] tested nickel-, copper-, and iron-enriched Zircaloy-2 samples under reactor conditions.

Results showed that increasing nickel caused a significant increase in hydrogen absorption, whereas copper and iron had little effect on the hydrogen absorption properties. In addition, hydrogen pickup was noted to increase under irradiation [3]. From these experiments, the authors concluded that nickel acted as a catalyst for surface reactions that allowed hydrogen to enter the oxide layer. However, because weight gains for these samples were not recorded, the hydrogen pickup fractions of the tested samples could not be compared with those of other experiments.

Recent results have indicated that Zircaloy-2 cladding exhibited increased HPUF at high burnup in a BWR [9]. This change in hydrogen pickup behavior was attributed to the dissolution of the finely distributed second-phase precipitates (SPPs) under irradiation [7,9]. More recent examinations of Zircaloy-2 structural components corroded in commercial BWRs and exposed to over 50 GWd/t burnup, exhibited wide variability in hydrogen pickup [7,10]. This change in hydrogen pickup behavior at high burnup was only observed in Zircaloy-2 components and not in Zircaloy-4. Fig. 1 shows the HPUF for Zircaloy-2 and Zircaloy-4 components in BWRs. It is clear that, at high burnup, Zircaloy-2 components show a wide range of HPUF, whereas the HPUF of Zircaloy-4 remains low. These results suggest that nickel may play an important role in this change in hydrogen pickup.

To discern the role of nickel in the hydrogen pickup process during irradiation, one property of particular interest is the oxidation state of nickel atoms upon their incorporation into the advancing oxide layer. Previous work has shown that iron and chromium are indeed noble with respect to zirconium and thus remain metallic

FIG. 1 Hydrogen pickup fraction of Zircaloy-2 and Zircaloy-4 components at high burnup in the boiling water reactor environment. Figure modified from Miyashita [10].

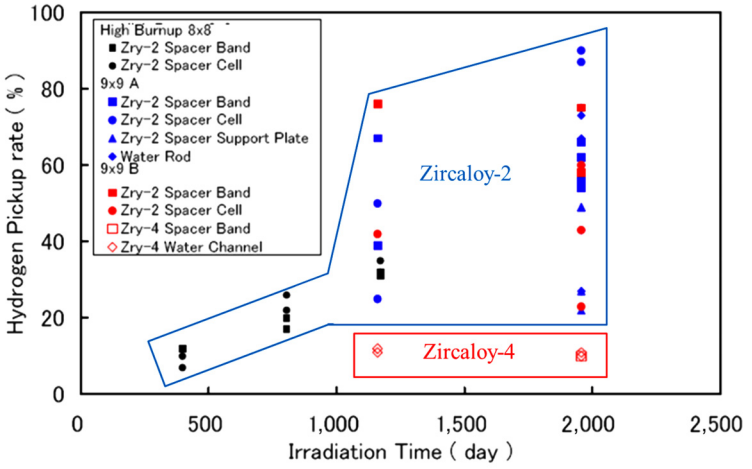

in Zircaloy-4 oxide layers formed in high-temperature autoclave environments [11–14]. To obtain information on the oxidation state of iron and nickel in a spatially resolved manner (i.e., as a function of distance from the interface), microbeam X-ray absorption near-edge spectroscopy (XANES) was used [11–12,15]. With this technique [performed at the Advanced Photon Source (APS) at Argonne National Laboratory], a microfocused X-ray beam was used to probe the oxide layer at the submicron level. Using cross-sectional samples of in-reactor–corroded material allowed for examinations as functions of distance from the oxide-metal interface.

Experimental Methods

MATERIALS

We chose a focused set of samples for this study to highlight the differences that lead to high hydrogen pickup of Zircaloy-2 in BWRs. To isolate the effect of heat flux, the samples were taken from water rods exposed to high fluence so that corrosion occurred under irradiation but in the absence of heat flux, except for the relatively small contribution from γ heating. Detailed descriptions of these irradiated samples are given in Table 1, and images of the water-rod samples are shown in Fig. 2. In addition, mean precipitate size and density for each sample are given in Table 2, as measured by Nippon Nuclear Fuel Development.

All materials were composed of Zircaloy-2 and underwent several α-annealing heat treatments that consisted of a vacuum annealing at 577°C after the β quench before

TABLE 1 Detailed descriptions of irradiated water-rod materials analyzed in this study.

Material	Archive 1	Material 10	Material 13	Material 17	Material 21
Water chemistry history	HWC/zinc/NM	HWC/zinc/NM	HWC/zinc/NM	HWC	HWC
Material type	Zircaloy-2	Zircaloy-2	Zircaloy-2	Zircaloy-2	Zircaloy-2
Composition at fabrication	Zr-1.29Sn-0.18Fe-0.10Cr-0.07Ni			Zr-1.55Sn-0.18Fe-0.12Cr-0.05Ni	
CAP (h)	2.19×10^{-19}	2.19×10^{-19}	2.19×10^{-19}	N/A	N/A
Fluence ($E > 1$ MeV) at sample elevation (10^{21} neutrons/cm^2)	~2	9.7	13.1	7.1	9.4
Inner-oxide thickness (μm)	N/A	22	29	3.0	9
Outer-oxide thickness (μm)	3.4	23	27	3.5	16
Hydrogen content (wt.ppm)	N/A	250	1,033	67	622
HPUF (%)	N/A	15	51	28	69
Exposure time (d)	2,036	2,036	2,703	1,665	2,193
Bundle average burnup (GWd/MTU)	59.7	59.7	74.6	32.8	43.7

Note: Reported oxide thicknesses are average values. Initial examinations were performed at the GEH Vallecitos Hot Cell Facility. CAP, cumulative annealing parameter; HPUF, hydrogen pickup fraction; HWC, hydrogen water chemistry; NM, noble metal.

FIG. 2 Post-irradiation pictures showing the appearance of irradiated reactor-exposed water-rod samples. Nodules of oxide are present on the surface of Material 17, indicating the occurrence of nodular corrosion. Images courtesy of Nippon Nuclear Fuel Development.

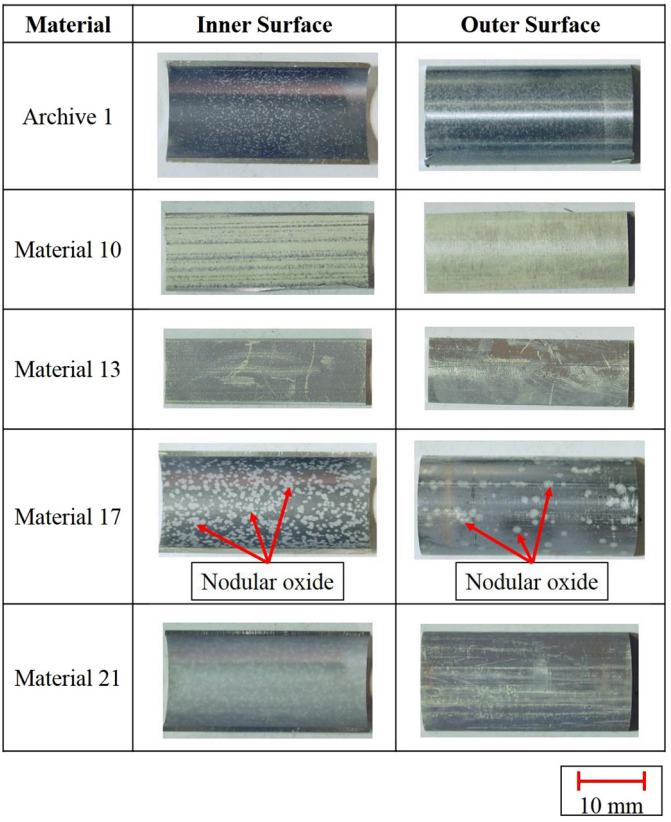

TABLE 2 Mean precipitate size and density for chromium- and nickel-rich precipitates.

	Archive 1	Material 10	Material 13	Material 17	Material 21
$Zr(Fe,Cr)_2$ precipitates					
Mean SPP diameter (nm)	56	52	59	81	73
Density (m^{-3})	1.78×10^{19}	1.64×10^{19}	1.60×10^{19}	1.27×10^{19}	1.19×10^{19}
$Zr_2(Fe,Ni)$ precipitates					
Mean SPP diameter (nm)	82	98	65	80	84
Density (m^{-3})	3.99×10^{18}	3.06×10^{18}	1.40×10^{18}	6.48×10^{17}	6.87×10^{17}

Note: Values courtesy of Nippon Nuclear Fuel Development. SPP, second-phase precipitate.

irradiation. Cumulative annealing parameters (CAP) for the different samples are shown in Table 1 and were calculated using a Q/R value of 40,000. Compositions given in Table 1 refer to nominal compositions at fabrication. The water chemistry history distinguishes between hydrogen water chemistry, the presence of zinc, and noble metal additions to the coolant. The surface temperature for all samples during the exposure was approximately 288°C, which is the saturation temperature in a BWR.

The samples in Table 1 are divided into two main sets. The first set compares two materials with similar oxide thicknesses but widely different HPUFs. Both materials were corroded in the Limerick-1 reactor, manufactured during the same production period, and irradiated in the core in symmetric locations for three 24-month cycles. The bundle from which Material 10 was taken was discharged, whereas the bundle from which Material 13 was taken was irradiated for one more cycle (24 months). Although the average outer-oxide thicknesses of Material 10 (low HPUF) and Material 13 (high HPUF) were 23 and 27 μm, respectively. Material 10 had an HPUF of 15 % and Material 13 had an HPUF of 51 %. From the as-irradiated precipitate size and density measurements given in Table 2, no significant difference in Laves-phase precipitate size and density was observed between Materials 10 and 13 post-irradiation. However, the size and density of nickel-containing precipitates in Material 13 was significantly smaller than in Material 10. However, because these values were measured using transmission electron microscopy (TEM), it is not known whether these differences were real or a result of measurement variability.

In the second set of samples, two materials were again compared. These samples were taken from water rods corroded in the Dresden-2 reactor. Material 17 (low HPUF: 28 %) exhibited an outer-oxide thickness of approximately 3.5 μm, and Material 21 (high HPUF: 69 %) exhibited an outer-oxide thickness of approximately 16 μm. Like the previous set of samples, these water rods were irradiated in symmetric fuel assemblies for three 24-month cycles. The assembly containing Material 17 was discharged after these three cycles, whereas the assembly containing Material 21 remained for an additional 24-month cycle. The as-irradiated precipitate sizes and densities for Materials 17 and 21 showed no significant difference in size or density for Laves-phase precipitates and nickel-containing precipitates (Table 2). A comparison of precipitate size and density between the first (Materials 10 and 13) and second (Materials 17 and 21) pairs showed that Materials 17 and 21 exhibited larger Laves-phase precipitates but at a lower density. In contrast, the nickel-containing precipitates of Materials 17 and 21 were of a similar size as Materials 10 and 13 but had a much lower density. Because the first set of samples underwent a different heat treatment than the second, initial precipitate size and distribution were different, so a comparison of as-irradiated precipitate sizes was not straightforward.

A fifth sample, called Archive 1, was taken from the bottom of the same water rod as Material 10. Although the neutron fluence at low elevations cannot be calculated precisely, it is estimated to be approximately 2×10^{21} neutrons/cm^2 ($E > 1$ MeV).

The sample was expected to have some irradiation damage, but because the fluence was low compared with that of the other samples located at higher elevations, the damage should have been substantially less. Therefore, the sample was assumed to be an indicator of thermal treatment effects only. Precipitate sizes for Archive 1 were comparable to those of Materials 10 and 13, while the densities of both types of precipitates were higher for Archive 1 than for Materials 10 and 13. This is consistent with the estimation that Archive 1 received a lower fluence than the other samples, and measurements in this sample were indicators of heat treatment effects only.

Oxide thicknesses for all samples except Archive 1 were measured using metallography at the GEH Vallecitos Hot Cell Facility, and oxide thickness measurements using microbeam synchrotron radiation in this study were consistent with metallographic examinations to approximately 5 μm. The oxide layers formed on the Zircaloy-2 materials in this study generally formed black shiny oxide layers. The oxide layers were generally uniform but displayed more variation than oxide layers formed on Zircaloy-4. Although Material 17 exhibited what appeared to be spots of nodular corrosion and Material 10 exhibited a lighter colored oxide, the oxide layers were protective and not spalling, so the weight gain and hydrogen pickup could be compared with that of the other samples in this study. Water rod samples were not de-crudded prior to examinations.

Hydrogen contents for all samples except Archive 1 were measured with a LECO RH-2 hydrogen analyzer, which uses an inert gas fusion method to release hydrogen. In this apparatus, the sample was melted in a graphite crucible containing a tin flux. The evolved hydrogen was swept from the crucible with high-purity nitrogen gas to a thermal conductivity detector, where the change in thermal conductivity of the gas stream was measured and related to the hydrogen content through a series of calibration standards.

SAMPLE PREPARATION

The samples for this study were shipped from the GEH Vallecitos Hot Cell Facility to the LAMDA laboratory at Oak Ridge National Laboratory (ORNL), where they were prepared as cross-sectional samples in a manner similar to previous work and briefly reviewed herein [11,16–17].

Cross-sectional TEM samples were prepared from the bulk material containing both metal and oxide. Two-millimeter-wide slices were cut from the bulk sample using a low-speed saw to yield one to two slices of each sample depending on the availability of the material. These two slices were placed in a slotted molybdenum rod with a 2-mm diameter. This assembly was placed in turn inside a 3-mm-diameter brass tube. EPOTEK-353ND epoxy was used to hold this structure in place. The molybdenum rods and brass tubes were selected for use because the elements that comprise those components (molybdenum, copper, and zinc) do not have X-ray fluorescence lines that overlap with those of the elements of interest (zirconium, iron, chromium, and nickel). EPO-TEK 353ND epoxy was chosen based on known performance and reliability [15–16].

Once the epoxy set, slices approximately 500-μm thick were cut from the tubular structure. After being cut, the samples were polished using successively finer grit, starting at 600 grits (16-μm particle size) and ending with a 1-μm diamond solution. An example optical micrograph of a completed cross-sectional sample is shown in Fig. 3. In addition, because samples were radioactive, they were encapsulated using 37-μm-thick polyimide tubing for synchrotron radiation examinations.

CHARACTERIZATION BY MICROBEAM XANES

XANES studies the absorption of X rays in a sample within approximately 30 eV from the absorption edge [18–20]. When an atom absorbs a photon, the ejected photoelectron can scatter from the electrons of the neighboring atoms. When the photoelectron energy is low (i.e., X-ray energy just above the absorption edge), the photoelectron is more likely to scatter from the electrons of multiple atoms in the structure [19,21]. After these scattering events, that photoelectron will be absorbed, and the absorbing atom will emit a characteristic X ray. Because the probability to reabsorb the photoelectron depends upon the availability of electronic states, the scattering events alter the intensity of the emitted characteristic X ray, which is measured in fluorescence XANES. As a result, the shape of a XANES spectrum gives information on the local structure of the element

FIG. 3 Example cross-sectional sample prepared for microbeam synchrotron radiation examinations from irradiated water-rod materials. The sample shown was prepared from Material 13. Samples were prepared and imaged at the LAMDA lab at Oak Ridge National Laboratory.

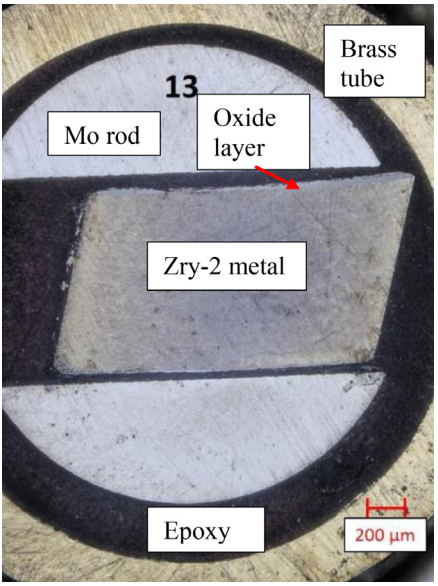

of interest, including oxidation state, coordination geometry, and metal-ligand orbital hybridization [19–21].

Because the shape of a XANES spectrum depends on the local atomic structure and oxidation state of the element of interest, one can expect a characteristic XANES spectrum for each element with a given electronic structure in a given phase. By characterizing and quantifying these differences, it is possible, in principle, to obtain the relative contributions of each phase present using well-characterized standards. To that end, standards were acquired based on the phases expected in the samples. The standards used in this study for the iron and nickel edges are listed in Table 3. Powder standards were obtained from Sigma-Aldrich and Alfa Aesar. The $Zr(Fe,Cr)_2$ standard was obtained by arc melting the three elements together at the given stoichiometry. The spectra for nickel in Zircaloy-2 were obtained by performing XANES on unoxidized Zircaloy-2 channel material. The pure metal nickel and iron standards were obtained from Hephaestus software, which is included in the Athena software package that was used for fitting [22]. These standards were modified for this data set by aligning edge positions to those of experimentally measured XANES spectra for face-centered cubic (fcc) nickel and body-centered cubic (bcc) iron powders; literature spectra and measured spectra were similar in shape and position, but literature standards were used because of their higher quality. The spectra for the experimental standards were later used in the oxidation state and linear combination fitting analyses.

SYNCHROTRON SETUP FOR MICROBEAM XANES

Microbeam XANES experiments were performed at the 2-ID-D beamline at the APS at Argonne National Laboratory. Using zone-plate diffraction gratings, an

TABLE 3 List of standards used for nickel and iron XANES examinations of Zircaloy-2.

Standards	Physical State	Origin
Nickel		
Face-centered cubic Ni	Foil/powder	Hephaestus/Sigma-Aldrich
Nickel in Zircaloy-2 metal	Bulk	Zircaloy-2 channel material
Nickel(II) oxide (NiO)	Powder	Sigma-Aldrich
Nickel(II,III) oxide ($Ni_{0.86}O$)	Powder	Alfa Aesar
Nickel(III) oxide (Ni_2O_3)	Powder	Sigma-Aldrich
Nickel ferrite ($NiFe_2O_4$)	Powder	Sigma-Aldrich
Iron		
Body-centered cubic Fe	Foil/powder	Hephaestus/Sigma-Aldrich
Fe in Laves-phase compound [$Zr(Fe,Cr)_2$]	Intermetallic compound	Arc-melted compound
Iron(II) oxide (FeO)	Powder	Sigma-Aldrich
Iron(II,III) oxide (Fe_3O_4)	Powder	Alfa Aesar
Iron(III) oxide (Fe_2O_3)	Powder	Sigma-Aldrich
Nickel ferrite ($NiFe_2O_4$)	Powder	Sigma-Aldrich

X-ray beam size of 0.2 by 0.2 μm (full width at half maximum) with a focal flux of 3×10^9 photons/s and an X-ray energy bandwidth (dE/E) of 0.01 % were obtained. A schematic of the experimental setup is shown in Fig. 4. In this geometry, the microbeam was incident on the sample at 76° from the sample normal, creating a footprint on the sample of 0.2 μm (normal to the oxide-metal interface) × 0.83 μm (parallel to oxide-metal interface). As a result of this geometry, the X-ray attenuation length into the sample was significantly reduced; using this geometry at 8.34 keV the attenuation length was 4.7 μm, whereas it would be 19.5 μm if the angle were 0° [23]. The sampling depth was considered to be three times this attenuation length, defined as the depth at which the X-ray intensity decreases by a factor of e^3 (approximately 95 % attenuation). Because the beam footprint was an oval with a major axis diameter of 0.83 μm and a minor axis diameter of 0.2 μm, the volume sampled by the beam at a particular point was approximately 7.4 μm^3. If nickel-containing precipitates are assumed, conservatively, to have a mean diameter of 200 nm and to be spherical, then the mean precipitate volume is approximately 4×10^{-3} μm^3, which is over three orders of magnitude smaller than the sampling volume. At the iron K-edge with 7.12 keV photons, the sampling volume is 4.8 μm^3, which is also three orders of magnitude larger than the precipitate volume. Because of this, the number of precipitates sampled by the beam was very large, and it was not possible to distinguish between nickel and iron in solid solution and in SPPs.

FIG. 4 Experimental setup for XANES experiments at the 2-ID-D beamline. As the scan moves from the metal into the oxide, (a) zirconium fluorescence and (b) XANES spectra are acquired. Numbered points in (a) and (b) are shown in (c).

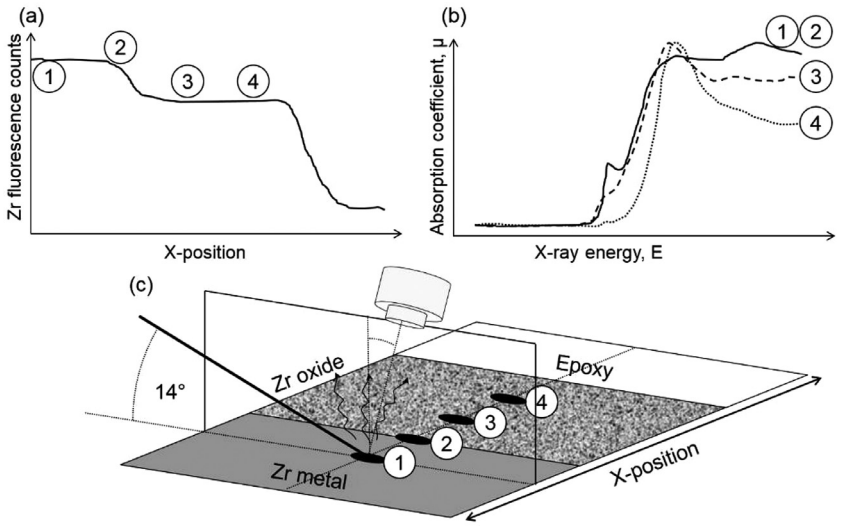

XANES signals were recorded in fluorescence, with a fluorescence detector placed near the sample normal. Each XANES scan probed the sample about the K-edge of the element of interest (8.34 keV for nickel and 7.12 keV for iron) with an energy window of ±40 eV and energy step of 0.5 eV, which is sufficient to resolve peaked structures at these absorption edges [18]. Although the beam size changes as the energy is changed during a XANES scan, this change was approximately only 1–2 %.

For each sample, the location of the oxide layer was determined by scanning the sample using zirconium L-edge fluorescence lines. As shown in **Fig. 4**, the plateau where zirconium fluorescence was the highest (1–2) was identified as the metal. The second plateau where zirconium fluorescence was slightly lower (3–4) was identified as the oxide layer. Similar fluorescence data for the other alloying elements were also collected. Once the oxide position had been determined, scans were set up to acquire XANES spectra at each point. Zirconium fluorescence data at each point were also recorded to ensure that the sample remained properly aligned. Iron K-edge XANES spectra were acquired at 1.5 s per energy point over the 80-eV range with a 0.5-eV step. Because of the low concentration of nickel in Zircaloy-2, data acquisition time was increased such that the number of counts in the XANES post-edge region was at least 3,000. All data were normalized to the incident beam intensity. In the metallic region of the sample (1–2), nickel and iron XANES measured in this region remained unchanged, whereas in the oxide region of the sample (3–4), XANES spectra began to change shape as nickel and iron began to transition from the metallic to the oxidized states.

ANALYSIS OF XANES SPECTRA

Once XANES data were acquired, they were imported into the Athena program for processing. The position of the absorption edge was calculated as the first position where the derivative of the fluorescence XANES absorption intensity with respect to energy was maximum. **Fig. 5** plots XANES spectra and their respective derivatives for fcc nickel and nickel(II) oxide. Edge positions were calculated as 8,332 and 8,340 eV for fcc nickel and nickel(II) oxide, respectively.

After this step in the data analysis, a pre-edge function was fit to the region before the absorption edge (e.g., $E < 8{,}315$ eV for nickel XANES), where absorption was minimal, whereas a post-edge function was fit to the region 15 eV past the edge position to the end of the acquired spectrum. Once these fits were completed, the spectrum was flattened to remove differences in the post-edge region from the data. This is especially useful when performing linear combination fitting [22].

Linear Combination Fitting

Spectra from the examined samples were fit to linear combinations of the spectra obtained from XANES standards. Because the distinction between oxide phases and metallic phases was much more marked than among individual metallic and oxide phases (as illustrated in the following section), the sum of each type of standard

FIG. 5 Edge position of XANES spectra as defined by the first maximum of the first derivative (shown in dotted lines). (a) XANES spectrum and derivative for fcc nickel and (b) the same for NiO.

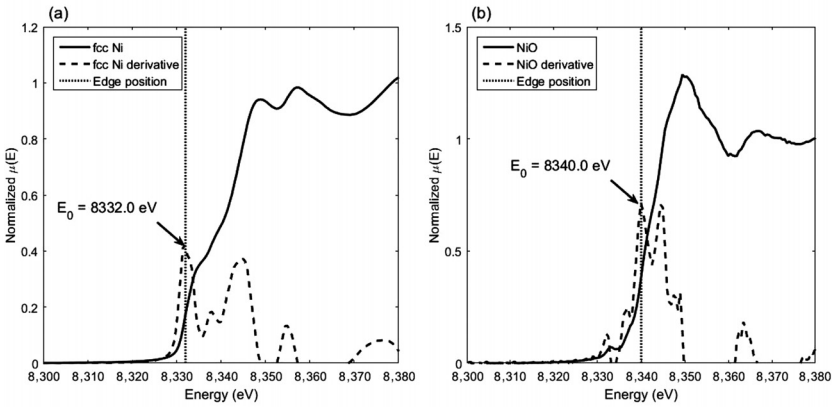

(i.e., all oxide phases versus all metallic phases) was used as a measure of oxidation state at any given point. Thus, the fraction of metallic nickel or iron was used to characterize the oxidation state of the alloying elements as a function of distance from the oxide-metal interface.

Correlation of Oxidation State with XANES Edge Position

Another analysis technique employed to examine the oxidation state of alloying elements was to relate XANES spectrum edge positions of the samples with those of the standard materials with a known oxidation state, as described in other XANES examinations of transition metal oxides [24]. This was performed to estimate the actual oxidation state of alloying elements within the oxide layer. This analysis technique is considered complementary to the linear combination fitting because the XANES edge position is more sensitive to the oxidation state than is the linear combination fitting.

Results

XANES SPECTRA

XANES spectra of the standard materials are shown in Fig. 6, where the normalized X-ray absorption coefficient is plotted as a function of energy for each standard material. Typical nickel XANES spectra acquired in the different samples are shown in Fig. 7, and typical iron XANES spectra are shown in Fig. 8.

Fig. 7 and Fig. 8 plot the normalized X-ray absorption coefficient as a function of energy for nickel and iron, respectively. Fig. 7a compares the fully metallic nickel XANES spectra of the samples with those of the metallic standards, and Fig. 7b does

FIG. 6 XANES spectra of standard materials used for fitting the acquired spectra. (a) Nickel XANES standards. (b) Iron XANES standards.

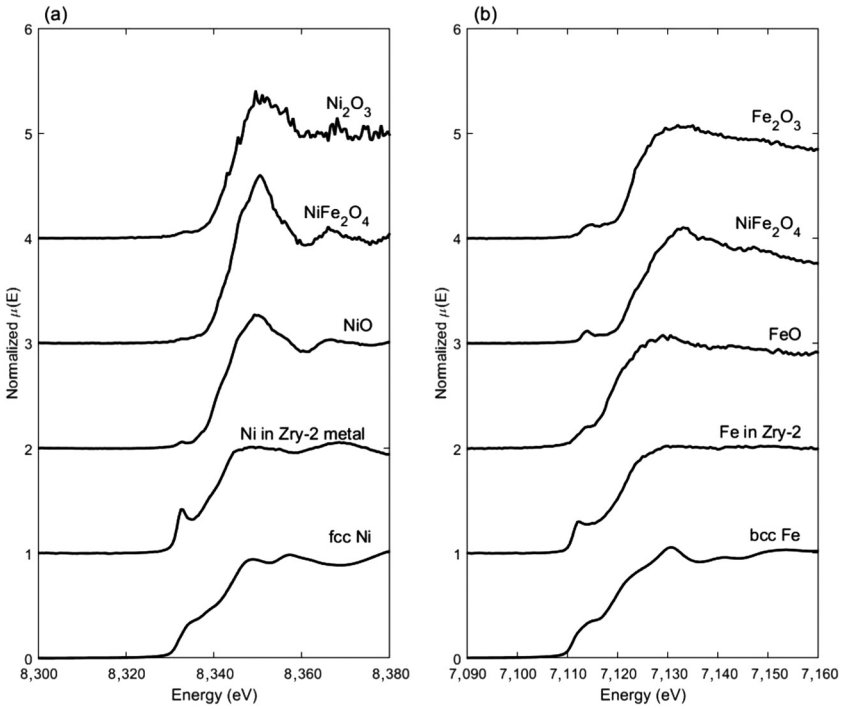

the same for the fully oxidized XANES spectra and standards. The metallic spectra in Fig. 7a are quite similar, and the same can be said of the oxide spectra in Fig. 7b. Fig. 8a compares the fully metallic iron XANES spectra of the samples with those of the metallic iron standards, and Fig. 8b compares the fully oxidized XANES spectra and standards. As in Fig. 7, the metallic spectra in Fig. 8a are quite similar, as well as the oxide spectra in Fig. 8b. Comparing the metallic and oxidized spectra of nickel and iron shows that spectra obtained in metallic Zircaloy-2 had a sharp feature at the metallic edge that was located at 7,112 eV for iron and 8,333 eV for nickel, called a rising-edge feature, and a relatively flat post-edge at energies above 7,130 eV for iron XANES and 8,345 eV for nickel XANES. In contrast, oxidized spectra exhibit a low-intensity pre-edge feature at 7,111.5 eV and 8,332.5 eV for iron and nickel XANES, respectively, and a high-intensity post-edge feature, often referred to as the white line, at 7,130 eV and 8,350 eV for iron and nickel XANES, respectively.

To better understand how XANES spectra changed shape and position as a function of oxide depth, the measured spectra at each spatial point in all samples was plotted, as shown in Fig. 9 for nickel XANES and Fig. 10 for iron XANES. These plots show the normalized X-ray absorption coefficient against X-ray energy and

FIG. 7 Nickel XANES spectra acquired from standards and samples. (a) Nickel XANES spectra from metallic standards and from the metal (far from the oxide-metal interface) of the analyzed samples. (b) Nickel XANES spectra from oxide standards and from the bulk oxide (1 μm from the oxide-water interface) of the analyzed samples.

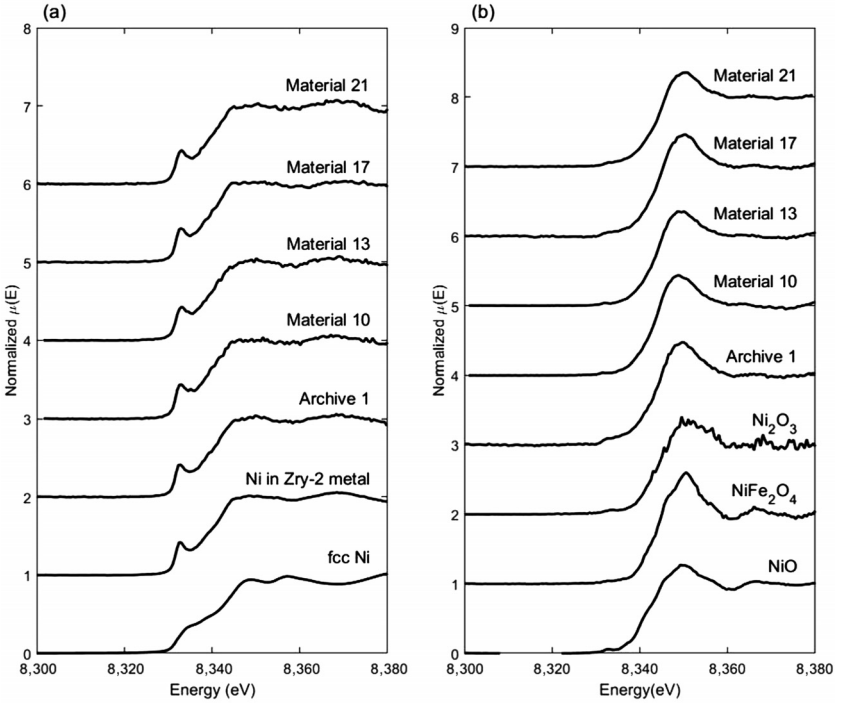

distance from the oxide-metal interface as determined by zirconium fluorescence and gives the evolution of the XANES spectra with oxide depth.

This type of analysis can be used to identify features that allow a qualitative evaluation of XANES measurements. For example, within a particular scan, it can be seen that in the metal the rising-edge feature remains constant. As the scan moves into the oxide layer, the rising-edge feature begins to decrease in intensity and reaches a constant minimum value. At the same time, the post-edge intensity (white line) increases and then reaches an approximately constant maximum. These features have been shown previously to be good indicators of changes in the oxidation state [12].

Fig. 9a shows the nickel XANES spectra for Archive 1 material. As one moves from the metal into the oxide layer, it is clear that the features described previously associated with the metallic phase decrease, whereas those associated with the oxide phase increase. In particular, the rising-edge feature intensity, associated with metallic nickel, decreases, whereas the intensity of the large post-edge feature (white

FIG. 8 Iron XANES spectra acquired from standards and samples. (a) Iron XANES spectra from metallic standards and from the metal (far from the oxide-metal interface) of the analyzed samples. (b) Iron XANES spectra from oxide standards and from the bulk oxide (1 μm from the oxide-water interface) of the analyzed samples.

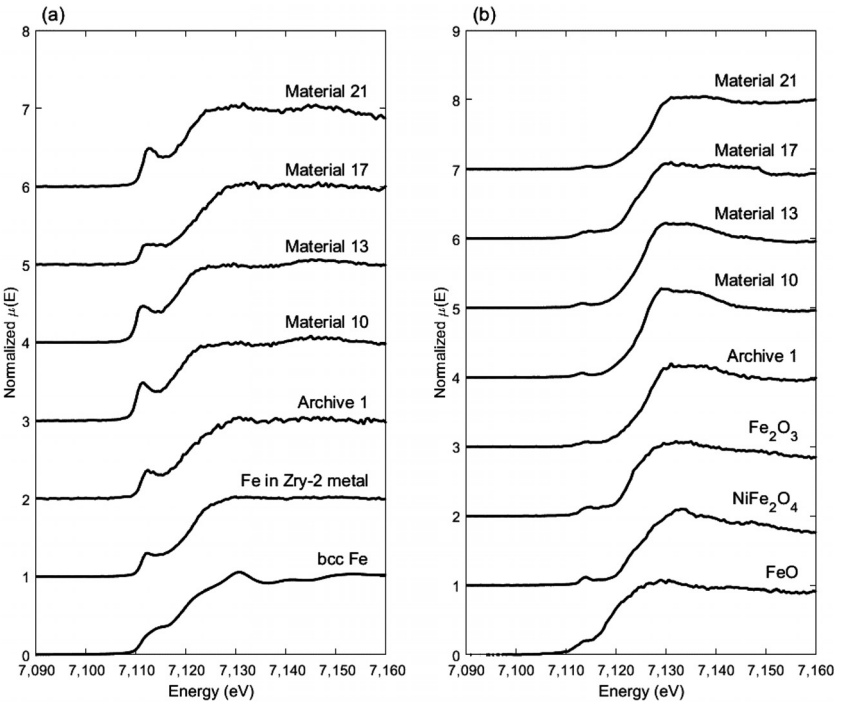

line), associated with oxidized nickel, increases. Not easily seen in Fig. 9 is the fact that the absorption-edge position also moves to a higher energy level as the nickel is oxidized. This is, to the first order, a Coulomb effect: higher oxidation states mean less charge on the atom, which results in less shielding of the nucleus. These changes in XANES features occur principally at the oxide-metal interface. However, it is noticeable in Fig. 9 that the rising-edge feature characteristic of metallic nickel remained in the oxide layer for a considerable distance (at least several micrometers) from the oxide-metal interface. This means that nickel did not oxidize immediately upon its incorporation in the oxide layer, with some metallic features remaining for approximately 2 μm. Note that Archive 1 and Material 17 oxide thicknesses were only 3.4 μm.

Nickel XANES spectra for Material 10 (Fig. 9b) and Material 17 (Fig. 9d) showed a similar permanence of metallic nickel spectrum characteristics that were clearly observed several micrometers into the oxide layer. In the thicker oxide layer

FIG. 9 Plots of nickel XANES spectra as a function of distance from the oxide-metal interface. (a) Results for Archive 1. (b) Results for Material 10. (c) Results for Material 13. (d) Results for Material 17. (e) Results for Material 21. Results are all plotted to reflect the same length scale. The dotted line shows the location of the oxide-water interface for each sample.

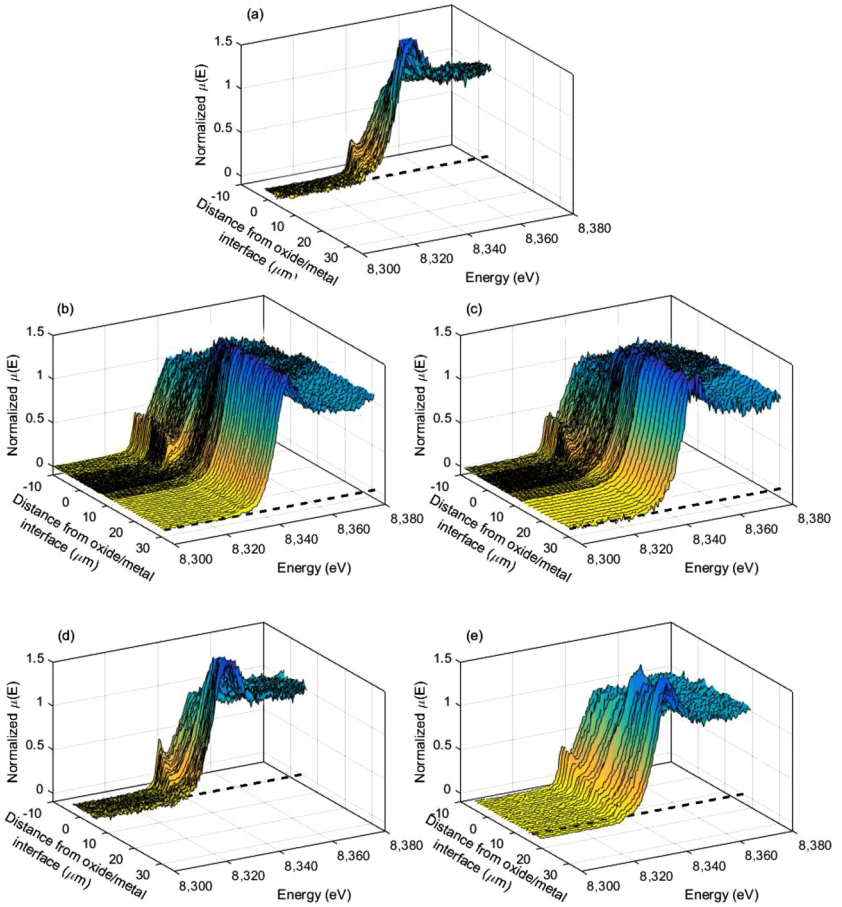

of Material 10, nickel exhibited metallic characteristics for up to 5 μm, whereas in Material 17, nickel exhibited metallic characteristics for approximately 3 μm, which, in this case, was the whole oxide thickness. As nickel transitioned from metallic to oxidized, the edge position of the XANES spectrum shifted to a higher energy.

XANES spectra for Material 13, shown in Fig. 9c, and Material 21, shown in Fig. 9e, also show metallic nickel at extended distances from the oxide-metal interface. In Material 13, nickel showed metallic characteristics for approximately 15 μm (approximately half the oxide thickness), whereas in Material 21, nickel exhibited

FIG. 10 Plots of iron XANES spectra as a function of distance from the oxide-metal interface. (a) Results for Archive 1. (b) Results for Material 10. (c) Results for Material 13. (d) Results for Material 17. (e) Results for Material 21. Results are all plotted to reflect the same length scale. The dotted line shows the location of the oxide-water interface for each sample.

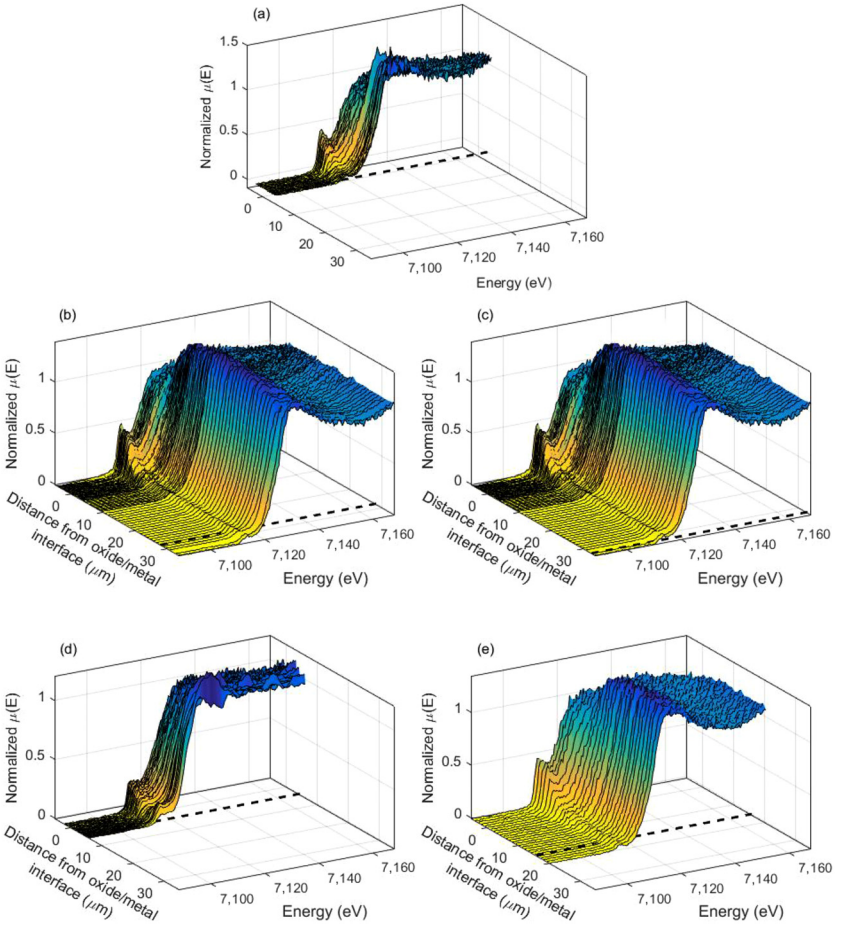

metallic characteristics right up to the oxide-water interface. Thus, it was observed that in the samples with higher hydrogen pickup nickel remained metallic further in the oxide layer compared with those with a lower HPUF.

Fig. 10a shows the iron XANES spectra for Archive 1. As for the nickel XANES spectra, as one moves from the metal into the oxide layer, the metallic phase characteristics, particularly the rising-edge feature, decrease, whereas those of the oxide phase, such as the high post-edge intensity, increase. As before, the X-ray absorption edge shifted to higher energy as the iron oxidized, and this transition from

metallic to oxidized characteristics occurred primarily near the oxide-metal interface. Iron also remained metallic for a distance into the oxide from the oxide-metal interface, typically on the order of approximately 2 μm in the thinner oxides of Archive 1 and Material 17, shown in Fig. 10d, and on the order of 5 μm in thicker oxides of Materials 10, 13, and 21, shown in Fig. 10b–d, respectively. Thus, no significant difference in iron oxidation was observed when comparing samples of low and high HPUFs, and the results were consistent with previous examinations of iron in Zircaloy-4 corroded in steam [12]. It should be noted that, for thinner oxides, points were evenly spaced using a step of at least 0.25 μm. The thick oxide layers were probed using a 1.0-μm step and a finer (0.25-μm step) mesh in the region near the oxide-metal interface.

LINEAR COMBINATION FITTING

A linear combination of the standard spectra was fit to the XANES spectra measured at a particular point in a sample. This was done for both nickel and iron XANES examinations of all samples using the standards detailed in Table 3. Example fits of nickel XANES spectra acquired from Material 10 are shown in Fig. 11.

FIG. 11 Nickel XANES linear combination fitting results for various points in Material 10. (a) Fitting results 10.2 μm from the oxide-metal interface in the metal. (b) Fitting results 2.8 μm from the oxide-metal interface in the oxide layer. (c) Fitting results 19.8 μm from the oxide-metal interface in the oxide layer.

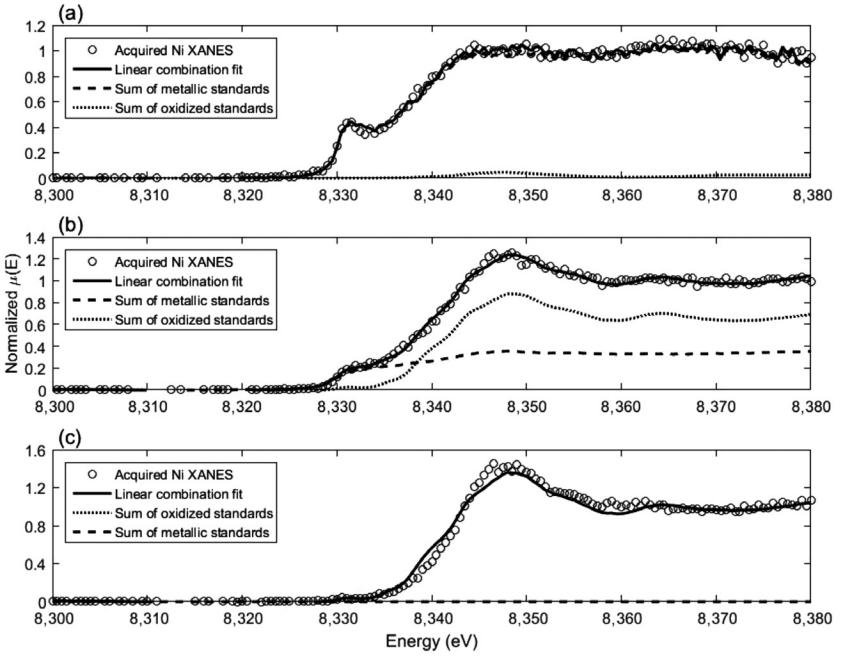

For each of these plots, the circles correspond to the acquired spectra and the solid lines correspond to the linear combination fitting. The dashed curves correspond to the sum of metallic standards and the dotted curves correspond to the sum of oxidized standards. Each fit had an associated R-factor. The R-factors found were consistently less than 0.01. The spectrum in **Fig. 11a** was acquired in the metal far from the oxide-metal interface, and it is clear that the fitting can be very well accomplished using only metallic standards. This was not the case for the spectrum in **Fig. 11b**, acquired in the oxide, not far from the oxide-metal interface, which can only be fitted with a combination of oxide and metal standards, as shown. Finally, the spectrum in **Fig. 11c** was acquired far from the oxide-metal interface into the oxide and can be fit using only oxide standards.

The fraction of metallic nickel at different locations in the oxide layer calculated from the sums of all oxide and metal phases is shown in **Fig. 12** and **Fig. 13**. The metallic nickel fraction is presented in **Fig. 12a** for each of the five samples examined. The oxide thicknesses are also indicated in each case. **Fig. 12b** shows the same data expanded near the oxide-metal interface.

The plots in **Fig. 12** indicate that in all samples studied nickel exhibited delayed oxidation relative to the host zirconium and remained metallic into the oxide layer. The percentage metallic nickel was much higher in the oxide layers associated with a high HPUF (Materials 13 and 21) than in those associated with a low HPUF (Archive 1 and Materials 10 and 17). This suggests that the presence of metallic nickel is important in increasing the HPUF. It is also apparent that, in Archive 1,

FIG. 12 Plot of metallic nickel weight fraction as a function of distance from the oxide-metal interface for each of the examined samples. (a) Linear combination fitting results over the whole oxide thickness range; (b) expanded view of results 15 μm near the oxide-metal interface.

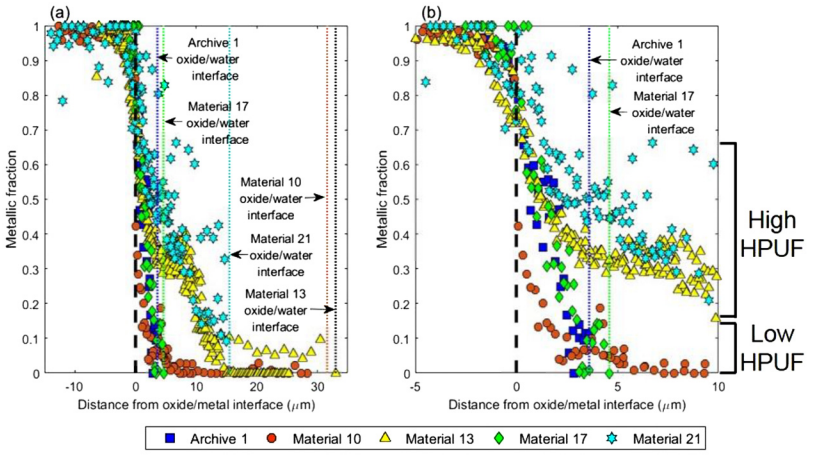

FIG. 13 Plot of metallic iron weight fraction as a function of distance from the oxide-metal interface for each of the examined samples. (a) Linear combination fitting results over the whole oxide thickness range; (b) expanded view of results 15 μm near the oxide-metal interface.

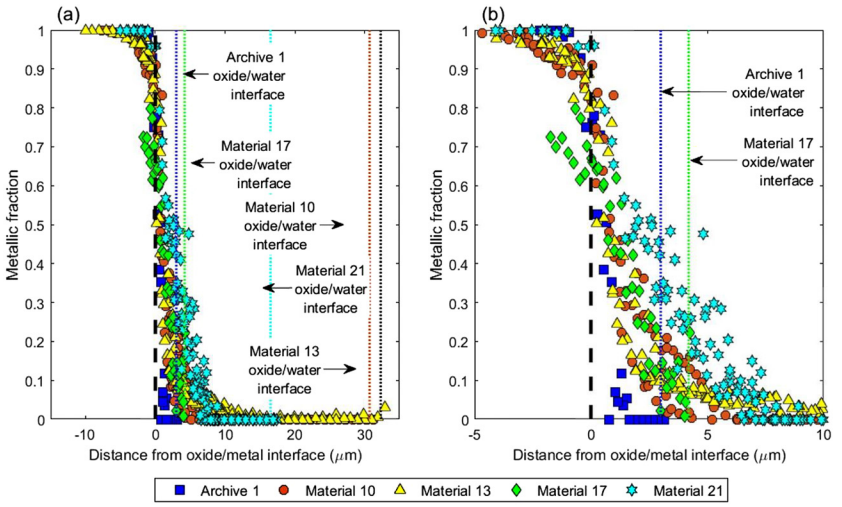

Material 17, and Material 10, nickel became fully oxidized less than 10 μm from the oxide-metal interface, whereas in Materials 13 and 21 (high HPUF), nickel remained partially metallic for a significant portion of the oxide thickness. In Material 13, nickel remained greater than 10 % metallic for approximately 15 μm away from the oxide-metal interface, whereas in Material 21, nickel only fully oxidized near the oxide-water interface. These fitting results were consistent with the evolution of the XANES spectra that was shown in Fig. 9.

Fig. 13 plots the same data but for the iron metallic fractions over the same set of samples. As in Fig. 12, Fig. 13a shows the data over the full range of oxide thickness, and Fig. 13b shows the same data over a region closer to the oxide-metal interface. Fig. 13 shows that the oxidation of iron was delayed relative to that of zirconium but earlier than that of nickel in each case. The remarkable observation was that iron showed no consistent difference in oxidation state between samples with high and low HPUFs. In Archive 1, iron fully oxidized within 2 μm from the interface, and in Materials 10 and 21 it fully oxidized within 5 μm. In Material 13, iron reached full oxidation by 10 μm from the interface. From these results, it is clear that nickel remained metallic longer than iron did and longer in materials with a high HPUF, whereas iron oxidation behavior between samples with high and low HPUFs was relatively similar. Some metallic iron was observed near the oxide-water interface in Material 17 and was assumed to be caused by the presence of iron from CRUD, which was mischaracterized as metallic iron. This was because

CRUD typically has a high concentration of iron, causing large detector dead times and misshapen XANES spectra because of self-absorption [25]. A similar, though smaller, variation in the nickel signal of Material 17 was also seen.

OXIDATION STATE ANALYSIS

The edge position as determined from the inflection point of the XANES spectrum is not used extensively in the linear combination fitting process but can be a more sensitive gage of the oxidation state because analyzing the oxidation state from the XANES edge position is independent of linear combination fitting. As described earlier, this analysis was performed by correlating the oxidation state of a standard with its XANES spectrum edge position. In this analysis, which took the edge of a particular spectrum as the maximum of the first derivative of the XANES spectrum, the edge energy was determined for each location in each sample. The standards and their oxidation states and XANES edge positions are shown in **Table 4**. Plots of the oxidation state as a function of the XANES edge position and best-fit lines for these plots are given in **Fig. 14**. The calibration curve for nickel and iron standards is shown in **Fig. 14a** and **b**, respectively. XANES edge positions in each of the XANES spectra at each point in each examined sample were calculated. The results of this analysis are shown in **Fig. 15**.

Fig. 15a plots the nickel XANES edge position as a function of distance from the oxide-metal interface. It can be seen that in all samples nickel oxidized to an oxidation state near 2+ (shown in the red band) around the oxide-metal interface and then further into the oxide layer to approximately 2.3+, which corresponded to a mixture of 70 % NiO and 30 % Ni_2O_3.

Fig. 15b plots iron XANES edge energy as a function of oxide depth. Iron appeared to oxidize to approximately the 3+ state (shown as the green band) near the oxide-metal interface and then to a higher oxidation state (possibly 4+) further

TABLE 4 List of XANES standards used for the calibration curves and their oxidation states and edge positions with respective 95 % CIs.

Standard	Oxidation State	Edge Position (eV) ± 95 % CI
Nickel		
Face-centered cubic	0+	8,331.9 ± 0.3
Nickel in Zry-2 metal	0+	8,331.0 ± 0.5
Nickel(II) oxide (NiO)	2+	8,340.0 ± 0.4
Nickel(II,III) oxide ($Ni_{0.86}O$)	2.32+	8,344.1 ± 0.2
Iron		
Body-centered cubic	0+	7,110.8 ± 1.0
Laves phase $Zr(Fe,Cr)_2$	0+	7,111.0 ± 0.2
Iron (II) oxide (FeO)	2+	7,117.9 ± 0.8
Iron(III) oxide (Fe_2O_3)	3+	7,122.8 ± 0.9

FIG. 14 Relations between oxidation states of standard materials to their XANES edge positions. Standards used are the ones listed in Table 4. (a) Relation for nickel standards; (b) relation for iron standards. Error bars are 95 % CIs of edge energy position.

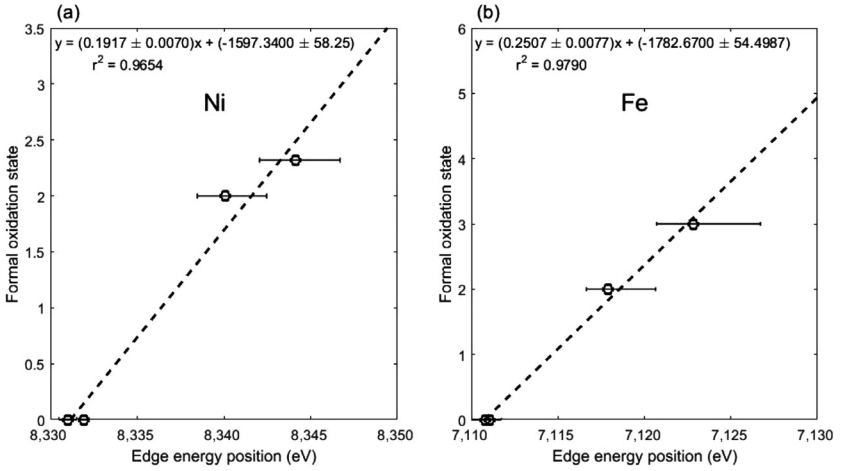

FIG. 15 XANES edge energies of (a) nickel and (b) iron as measured using the maximum of spectrum derivative. Boxed regions show edge position ± 95 % CIs for standard materials.

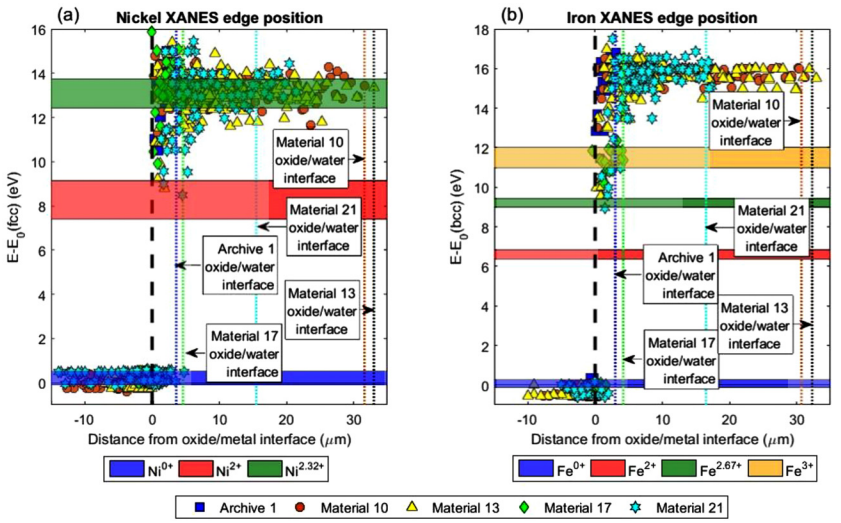

away. The only sample for which this was not the case was Material 17, in which iron remained in the 3+ state throughout the thin oxide layer.

Discussion

RELATION BETWEEN DELAYED OXIDATION OF ALLOYING ELEMENTS AND HYDROGEN PICKUP

Both nickel and iron exhibited delayed oxidation relative to the base zirconium. The delayed oxidation of iron was in agreement with previous examinations of Zircaloy-4 oxide layers using both electron microscopy and XANES [11,12,26–29]. Based on the work by Pêcheur et al. [26,27], it is believed that there are different domains of stability for zirconium, iron, and chromium in the metallic state in the dense oxide layer. Thus, when precipitates are initially incorporated into the oxide layer, they remain metallic because they are more thermodynamically noble than the base zirconium metal [14]. As the oxide grows inward, the partial pressure of oxygen experienced by the metallic precipitate begins to increase, causing the oxidation of (in order) zirconium, chromium, and iron [26]. Extending this argument to include nickel indicates that nickel will remain metallic longer than the other alloying elements because it is known to be more thermodynamically immune to corrosion in water than the other elements in zirconium-based alloys [30]. This is consistent with observations in this experiment, which showed that nickel did, in fact, remain metallic longer than did iron, as shown by a comparison of **Fig. 12** and **Fig. 13**. It should be noted that because these measurements were performed in 500-μm-thick samples, it was not possible to distinguish the contributions of nickel and iron in solid solution from that of nickel and iron in precipitates [11].

Comparing the results of iron oxidation behavior in this study to the results of previous examinations of iron in autoclave-corroded Zircaloy-4 shows that iron in BWR-corroded Zircaloy-2 remains metallic for up to 5 μm past the oxide-metal interface into the oxide layer, whereas iron in autoclave-corroded Zircaloy-4 remains metallic up to approximately 1.5 μm in 360°C water and 5–6 μm in 400°C steam [11,12]. Ensor et al. [12] hypothesized that iron remained metallic longer in steam-corroded samples than in water-corroded samples because, for a given oxide thickness, the faster corrosion kinetics at higher temperatures allow less time for iron to oxidize. For the samples examined in this study, no clear effect of iron oxidation on hydrogen pickup was discernable.

A consistent difference was seen in the oxidation behavior of nickel between low- and high-HPUF materials. A comparison of metallic nickel fraction in Materials 10 (low HPUF) and 13 (high HPUF) showed that nickel remained metallic longer in Material 13 than in Material 10. Although in Material 10 nickel began to oxidize later than iron, both elements became fully oxidized at approximately the same point, which was 5 μm from the oxide-metal interface in the oxide layer. In Material 13, both nickel and iron began to oxidize at approximately the same point that corresponded to the oxide-metal interface. However, whereas iron behaved in

a similar manner as in Material 10, nickel remained partially metallic for more than 10 μm past the oxide-metal interface into the oxide layer.

A comparison between Materials 17 (low HPUF) and 21 (high HPUF) paralleled the previous comparison. In Material 17, the oxidation behaviors of iron and nickel were similar to what they were in Material 10. In Material 21, iron and nickel began to oxidize at the same point, close to the oxide-metal interface. However, whereas iron reached approximately complete oxidation at approximately 5 μm from the oxide-metal interface, nickel remained partially metallic for more than 10 μm past the interface. From these results, it is clear that nickel remained metallic in the high-HPUF samples for a thickness larger than the protective oxide layer, which is typically between 2–3 μm in Zircaloy-2 corroded in a steam environment [8]. Thus, metallic nickel would be present in the porous oxide layer, allowing the corrosion medium access to the metallic nickel. Because of this, it is hypothesized that metallic nickel acts as a catalyst for surface reactions that result in hydrogen ingress from the coolant to the protective oxide layer. However, the mechanism by which nickel remains metallic to such distances in the oxide layers of high-HPUF samples is not fully understood.

An examination of the results from Archive 1 showed that nickel became fully oxidized approximately 2.5–3 μm from the oxide-metal interface, whereas iron became fully oxidized within 2 μm of the interface. This analysis suggests that delayed oxidation of nickel in the zirconium-oxide layer plays a role in accelerated hydrogen pickup of Zircaloy-2 at high burnup. In particular, samples with significantly delayed oxidation of nickel exhibited high hydrogen pickup.

The observations shown herein raise the question of how nickel affects hydrogen pickup in zirconium alloys. The possibility of metallic nickel enhancing hydrogen transport in the oxide layer has been raised by some researchers because the presence of a metallic nickel "short circuit" could allow easier hydrogen ingress [7]. However, such a short-circuit path would also lead to easier electron transport from the metal out of the oxide layer, which would cause hydrogen evolution at the oxide-water interface, thus reducing hydrogen pickup [15,31,32]. One possibility is that the presence of metallic nickel in the outer portion of the protective oxide layer and at the pore surfaces of the nonprotective oxide could enhance hydrogen ingress into the oxide, thus acting as a catalyst for the surface reaction. This could be consistent with higher hydrogen pickup in samples in which metallic nickel is present in larger quantities at larger distances in the oxide layer. Because de-crudding was performed, it is possible that crud present on the outer oxide surface could affect the corrosion potential and thus hydrogen pickup, but the mechanism by which this would occur is not known.

CHEMICAL STATE OF ALLOYING ELEMENTS UPON INCORPORATION INTO OXIDE LAYER

Because previous investigations of SPP corrosion behavior in Zircaloy-4 saw evidence for the presence of bcc iron [26], nickel and iron XANES spectra were fit

to include fcc nickel and bcc iron as standards. The case of fcc nickel is shown in Fig. 11b, which suggests the presence of a phase akin to fcc nickel as well as bcc iron in the samples. In fitting the XANES spectra in the oxide, it is often found that the inclusion of fcc nickel and/or bcc iron as standards is essential to achieving a good fit. Fitting weights for these standards are especially high near the region where nickel and iron transitioned from the metallic to the oxidized state. In the metal, although bcc iron and fcc nickel standards can be included with small-fitting weight fractions in the fit, they are not necessary. In analyzing the fluorescence spectra acquired above the nickel K-edge from scans of the oxide layer, it was noticeable that iron peaks were normally found near both chromium and nickel peaks, suggesting the presence of precipitates in those locations. An increase in nickel fluorescence count rate was also correlated with the presence of fcc nickel, in qualitative agreement with the determination of bcc iron found within ZrCrFe precipitates in the oxide layer [26], although it was not possible to definitively assign fcc nickel to the intermetallic precipitates.

From the results of the oxidation state analysis of nickel, it appears that nickel oxidized to approximately the 2.3+ state, corresponding to a mixture of 70 % NiO and 30 % Ni_2O_3. The correlation between the oxidation state and edge position for iron shows that, in Archive 1 and Materials 10, 13, and 21, the oxidation state was approximately 3+ near the oxide-metal interface and a higher state further into the oxide layer. This suggests that iron initially corroded to Fe_2O_3 in the oxide layer and then formed a mixture of phases, such as Fe_2O_3 and FeO_2.

Previous work has predicted that in oxidizing conditions in the zirconium oxide layer the stable oxidation states for nickel and iron were both 3+ [34]. However, FeO_2 has been observed in studies of the oxidation of iron metal in an oxygen-doped argon matrix under ultraviolet irradiation, and other similar oxides, such as Fe_2O_4, Fe_2O_5, and Fe_2O_6, have been reported to form during the interaction between laser-ablated iron and oxygen, thus showing that iron is capable of oxidizing up to the 6+ state, albeit under extreme conditions [35,36].

Conclusions

A focused set of neutron-irradiated Zircaloy-2 water-rod samples was examined to highlight the differences that lead to accelerated hydrogen pickup at high burnup. Measurements of nickel and iron oxidation state as spatially resolved within the oxide depth were conducted using microbeam synchrotron radiation XANES for each of these samples. Measured XANES spectra were compared with spectra of standard materials to obtain information on the oxidation behavior of iron and nickel once incorporated into the oxide layer. The main conclusions are as follows:

1. Zirconium, iron, and nickel oxidized in this order, consistent with Pourbaix diagrams of the three elements in which nickel is ranked as the most thermodynamically noble of the three elements and zirconium the least.
2. In samples with low HPUF, nickel began to oxidize later than did iron, but both reached approximately full oxidation near the same position. In contrast,

in the samples with high HPUF, nickel and iron both began to oxidize at the same point. Iron oxidized in a similar fashion in both low- and high-HPUF materials, whereas nickel remained partially metallic for significant portions of the oxide thickness in high-HPUF materials. This suggests that the presence of metallic nickel in the nonprotective oxide layer could have been a reason for higher hydrogen pickup in these alloys.

3. The oxidation state of nickel in the oxide layers was determined to be approximately 2+ near the oxide-metal interface and approximately 2.3+ further into the oxide layer, suggesting a mixture of 70 % NiO and 30 % Ni_2O_3. In contrast, iron initially oxidized to 3+, increasing later in the oxide layer. Linear combination fitting indicated the presence of fcc nickel and bcc iron at particular locations in the oxide.

ACKNOWLEDGMENTS

This research was funded by the Electric Power Research Institute-led Nuclear Fuel Industry Research (NFIR) program. We thank the NFIR members for their technical input and permission to publish the results. We acknowledge the resources provided by the 2-ID-D beamline staff and APS safety officers, especially W. VanWingeren, for accommodations to examine radioactive samples at the 2-ID-D beamline. We thank the staff at GEH Vallecitos Nuclear Center for shipping radioactive samples to ORNL for preparation and acknowledge the resources provided by the staff at the LAMDA laboratory at ORNL, including J. Busby and I. Dunbar for help in preparing the samples and shipping them to APS. We thank A. Couet, K. Sakamoto, G. Kuri, N. Ramasubramanian, F. Garzarolli, M. Newville, and B. Ravel for helpful discussions. Finally, we thank B. Ensor, E. Lacroix, and E. Alat for their assistance in performing experiments at the APS. This research used resources of the APS, a U.S. Department of Energy Office (DOE) of Science User Facility operated for the DOE Office of Science by Argonne National Laboratory under Contract No. DE-AC02-06CH11357.

References

[1] Lustman, B., "Zirconium Technology—Twenty Years of Evolution," *Zirconium in the Nuclear Industry, ASTM STP681*, J. H. Schemel and T. P. Papazoglou, Eds., ASTM International, West Conshohocken, PA, 1979, pp. 5–18.

[2] Kass, S., "The Development of Zircaloys," *Corrosion of Zirconium Alloys, ASTM STP368*, W. Anderson, Ed., ASTM International, West Conshohocken, PA, 1964, pp. 3–27.

[3] Yeniscavich, W., Wolfe, R. A., and Lieberman, R. M., "Hydrogen Absorption by Nickel Enriched Zircaloy-2," *J. Nucl. Mater.*, Vol. 1, No. 3, 1959, pp. 271–280.

[4] Harada, M., Kimpara, M., and Abe, K., "Effect of Alloying Elements on Uniform Corrosion Resistance of Zirconium-Based Alloys in 360°C Water and 400°C Steam," *Zirconium in the Nuclear Industry: Ninth International Symposium, ASTM STP1132*, C. M. Eucken and A. M. Garde, Eds., ASTM International, West Conshohocken, PA, 1991, pp. 368–390.

[5] Broy, Y., Garzarolli, F., Seibold, A., and Swam, L. F. V., "Influence of Transition Elements Fe, Cr, and V on Long-Time Corrosion in PWRs," *Zirconium in the Nuclear Industry: Twelfth International Symposium, ASTM STP1354*, G. P. Sabol and G. D. Moan, Eds., ASTM International, West Conshohocken, PA, 2000, pp. 609–622.

[6] Baur, K., Garzarolli, F., Ruhmann, H., Sell, H. J., Harbottle, J., Elmoselhi, M., Cheng, B., and Maguire, M., "Electrochemical Examinations in 350 Degrees C Water with Respect to the Mechanism of Corrosion-Hydrogen Pickup," *Zirconium in the Nuclear Industry: Twelfth International Symposium, ASTM STP1354*, G. P. Sabol and G. D. Moan, Eds., ASTM International, West Conshohocken, PA, 2000, pp. 836–852.

[7] Garzarolli, F., Cox, B., and Rudling, P., "Optimization of Zry-2 for High Burnups," *Zirconium in the Nuclear Industry: 16th International Symposium, ASTM STP1529*, M. Limbäck and P. Barbéris, Eds., ASTM International, West Conshohocken, PA, 2011, pp. 711–727.

[8] Kass, S. and Kirk, W. W., "Corrosion and Hydrogen Absorption Properties of Nickel-Free Zircaloy-2 and Zircaloy-4," *ASM Trans.*, Vol. 55, No. 1, 1962, pp. 77–100.

[9] Huang, P. Y., Mahmood, S. T., and Adamson, R. B., "Effects of Thermomechanical Processing on In-Reactor Corrosion and Post-Irradiation Mechanical Properties of Zircaloy-2," *Zirconium in the Nuclear Industry: Eleventh International Symposium, ASTM STP1295*, E. R. Bradley and G. P. Sabol, Eds., ASTM International, West Conshohocken, PA, 1996, pp. 726–755.

[10] Miyashita, T., Nakae, N., Ogata, K., Baba, T., Kamimura, K., Matsumoto, T., and Kakiuchi, K., "Corrosion and Hydrogen Pickup Behaviors of Cladding and Structural Components in BWR High Burnup 9×9 Lead Use Assemblies," presented at *LWR Fuel Performance/Top Fuel*, San Francisco, CA, September 30–October 3, 2007, American Nuclear Society, La Grange Park, IL, 2007, pp. 401–408.

[11] Couet, A., Motta, A. T., De Gabory, B., and Cai, Z., "Microbeam X-Ray Absorption Near-Edge Spectroscopy Study of the Oxidation of Fe and Nb in Zirconium Alloy Oxide Layers," *J. Nucl. Mater.*, Vol. 452, Nos. 1–3, 2014, pp. 614–627.

[12] Ensor, B., Motta, A. T., Bajaj, R., Seidensticker, J. R., and Cai, Z., "XANES Analysis of Iron in Zircaloy-4 Oxides Formed at Different Temperatures Studied with Microbeam Synchrotron Radiation," presented at *LWR Fuel Performance/Top Fuel*, Zurich, Switzerland, September 13–17, 2015, American Nuclear Society, La Grange Park, IL, 2015, pp. 13–17.

[13] Sakamoto, K., Une, K., and Aomi, M., "Chemical State of Alloying Elements in Oxide Layer of Zr-Based Alloys," presented at *LWR Fuel Performance Conference/Top Fuel/WRFPM*, Orlando, FL, September 26–29, 2010, American Nuclear Society, La Grange Park, IL, 2010, pp. 101–106.

[14] Gulbransen, E. A. and Andrew, K. F., "Oxidation Studies on Zirconium Alloys in High-Pressure Liquid Water at 360°C," *J. Electrochem. Soc.*, Vol. 116, No. 5, 1969, pp. 659–664.

[15] Couet, A., Motta, A. T., and Comstock, R. J., "Effect of Alloying Elements on Hydrogen Pickup in Zirconium Alloys," *Zirconium in the Nuclear Industry: 17th Volume, ASTM STP1543*, B. Comstock and P. Barbéris, Eds., ASTM International, West Conshohocken, PA, 2015, pp. 479–514.

[16] Yilmazbayhan, A., Motta, A. T., Comstock, R. J., Sabol, G. P., Barry, L., and Zhonghou, C., "Structure of Zirconium Alloy Oxides Formed in Pure Water Studied with Synchrotron Radiation and Optical Microscopy: Relation to Corrosion Rate," *J. Nucl. Mater.*, Vol. 324, No. 1, 2004, pp. 6–22.

[17] Motta, A. T., Da Silva, M. J. G., Yilmazbayhan, A., Comstock, R. J., Cai, Z., and Lai, B., "Microstructural Characterization of Oxides Formed on Model Zr Alloys Using Synchrotron Radiation," *Zirconium in the Nuclear Industry: 15th International Symposium, ASTM STP1505*, B. Kammenzind and M. Limbäck, Eds., ASTM International, West Conshohocken, PA, 2009, pp. 486–506.

[18] Frahm, R., "New Method for Time Dependent X-Ray Absorption Studies," *Rev. Sci. Instr.*, Vol. 60, No. 7, 1989, pp. 2515–2518.

[19] Als-Nielsen, J. and McMorrow, D., *Elements of Modern X-Ray Physics*, Wiley, London, 2011.

[20] Sarangi, R., "X-Ray Absorption Near-Edge Spectroscopy in Bioinorganic Chemistry: Application to M–O(2) Systems," *Coord. Chem. Rev.*, Vol. 257, No. 2, 2013, pp. 459–472.

[21] Ravel, B., "A Practical Introduction to Multiple Scattering Theory," *J. Alloys Compounds*, Vol. 401, Nos. 1–2, 2005, pp. 118–126.

[22] Ravel, B. and Newville, M., "ATHENA, ARTEMIS, HEPHAESTUS: Data Analysis for X-Ray Absorption Spectroscopy Using IFEFFIT," *J. Synchroton. Radiat.*, Vol. 12 (Pt 4), 2005, pp. 537–541.

[23] Henke, B. L., Gullikson, E. M., and Davies, J. C., "X-Ray Interactions: Photoabsorption, Scattering, Transmission and Reflection at E = 50–30,000 eV, Z = 1–92," *Atom. Data Nucl. Data Tables*, Vol. 54, No. 2, 1993, p. 349.

[24] Ravel, B., Scorzato, C., Siddons, D. P., Kelly, S. D., and Bare, S. R., "Simultaneous XAFS Measurements of Multiple Samples," *J. Synchr. Rad.*, Vol. 17, No. 3, 2010, pp. 380–385.

[25] Castelli, R. A., "The Corrosion Source," *Nuclear Corrosion Modelling*, Butterworth-Heinemann, Boston, 2009, pp. 1–31.

[26] Pêcheur, D., Lefebvre, F., Motta, A. T., Lemaignan, C., and Wadier, J. F., "Precipitate Evolution in the Zircaloy-4 Oxide Layer," *J. Nucl. Mater.*, Vol. 189, No. 3, 1992, pp. 318–332.

[27] Pêcheur, D., Lefebvre, F., Motta, A. T., Lemaignan, C., and Charquet, D., "Effect of Irradiation on the Precipitate Stability in Zr Alloys," *J. Nucl. Mater.*, Vol. 205, 1993, pp. 445–451.

[28] De Gabory, B., Motta, A. T., and Wang, K., "Transmission Electron Microscopy Characterization of Zircaloy-4 and ZIRLO Oxide Layers," *J. Nucl. Mater.*, Vol. 456, 2015, pp. 272–280.

[29] Hatano, Y., Isobe, K., Hitaka, R., and Sugisaki, M., "Role of Intermetallic Precipitates in Hydrogen Uptake of Zircaloy-2," *J. Nucl. Sci. Tech.*, Vol. 33, No. 12, 1996.

[30] Pourbaix, M. and Staehle, R. W., *Lectures on Electrochemical Corrosion*, Springer, New York, 1973.

[31] Couet, A., Motta, A. T., Comstock, R. J., and Ambard, A., "Oxide Electronic Conductivity and Hydrogen Pickup Fraction in Zr Alloys," presented at *ANS Annual Meeting*, Reno, NV, June 15–19, 2014, American Nuclear Society, La Grange, IL, 2014.

[32] Couet, A., Motta, A. T., and Comstock, R. J., "Hydrogen Pickup Measurements in Zirconium Alloys: Relation to Oxidation Kinetics," *J. Nucl. Mater.*, Vol. 451, Nos. 1–3, 2014, pp. 1–13.

[33] Motta, A. T., Yilmazbayhan, A., Comstock, R. J., Partezana, J., Sabol, G. P., Lai, B., and Cai, Z., "Microstructure and Growth Mechanism of Oxide Layers Formed on Zr Alloys Studied with Micro-Beam Synchrotron Radiation," *Zirconium in the Nuclear Industry: Fourteenth International Symposium, ASTM STP1467*, P. Rudling and B. Kammenzind, Eds., ASTM International, West Conshohocken, PA, 2005, pp. 1–26.

[34] Harding, J. H., "The Effect of Alloying Elements on Zircaloy Corrosion," *J. Nucl. Mater.*, Vol. 202, No. 3, 1993, pp. 216–221.

[35] Chang, S., Blyholder, G., and Fernandez, J., "Iron-Oxygen Interactions in an Argon Matrix," *Inorg. Chem.*, Vol. 20, No. 9, 1981, pp. 2813–2817.

[36] Xue, W., Yin, S., Ding, X. L., He, S. G., and Ge, M. F., "Ground State Structures of Fe(2)O(4-6)(+) Clusters Probed by Reactions with N(2)," *J. Phys. Chem. A*, Vol. 113, No. 18, 2009, pp. 5302–5309.

Discussion

Questions from Javier Romero, Westinghouse Electric Company:

1. Please comment on the role of nickel on recombination of hydrogen into H_2 compared with beneficial elements such as iron (see work from Lindgren and Panas).
2. What is the morphology and location of the metallic nickel that remains? Does the endurance of metallic nickel have anything to do with SPP size/distribution?

Authors' Response:

1. We believe that nickel enhances hydrogen pickup by serving as a catalyst for the surface absorption reaction. To our knowledge, iron does not enhance hydrogen pickup.
2. We do not know the location of the metallic nickel detected, whether it is in precipitates, matrix, etc. This would be an interesting area for further studies.

Question from Hans-Olof Andrén, Chalmers University of Technology:—There are two families of SPPs in Zircaloy-2: chromium-rich and usually somewhat bigger nickel-rich. As soon as they lose contact with the metal because of the inwardly growing oxide they will start to oxidize, but this oxidation may take quite some time, especially for the nickel-rich SPPs. Iron is oxidized first and leaves the SPP; later, when the oxygen potential is high enough, nickel will also oxidize. I suggest that the observation of metallic nickel in the oxide far from the oxide-metal interface stems from the remnants of such SPPs. Do you know the mean size of the two SPP families in the various materials?

Authors' Response:—We do not fully agree with the statement and believe that metallic Cr-rich precipitates may exist in the oxide layer even after losing contact with the matrix. The precipitate size and density has been studied for these materials. The diameter range was 56–73 nm for chromium-rich precipitates and 65–98 nm for nickel-rich precipitates. It is possible that the metallic nickel is in the remnants of precipitates, but we have no information on it at this point.

Question from Chris Grovenor, University of Oxford:—What form do you think the unoxidized nickel that you detect was in? You comment that nickel in the oxide might have doped it and increased conductivity, but this could only be true if it was in solution in the oxide and created an electronic state near enough to conduction and valence band edge to be ionized at 300°C. Only Ni^{2+} can do this, but the states are deep. Ni° in undissolved SPPs are likely to be too far apart to influence macroscopic conductivity, so how do you think that Ni° can have an effect on conductivity?

Authors' Response:—As stated above we do not know what form the metallic nickel was in. We agree with you that the Ni effect is not on enhancing conductivity or otherwise enhancing transport but rather in enhancing the surface reaction of hydrogen absorption by the oxide from the coolant.

Comment from Johannes Bertsch, Paul Scherrer Institute:—At Paul Scherrer Institute, we have found with synchrotron XAFS that larger nickel-containing SPPs are not fully oxidized. Such remnants of precipitates can explain the different spectra and behaviors that you presented.

Authors' Response:—As stated previously, this is quite possible.

Questions from Doug Rishel, Bechtel Marine Propulsion Corporation:

1. For the samples you examined, what were the BWR reactor water chemistries?
2. If available, are there any plans to examine Zircaloy-2 samples from materials exposed to PWR water chemistries?

Authors' Response:

1. For Archive 1, Material 10, and Material 13, reactor water chemistry was hydrogen water chemistry with additions of noble metals and zinc. For Materials 17 and 21, the reactor water chemistry was hydrogen water chemistry only.
2. We have no current plans to do so, but it would be an interesting study to perform.

Question from Pierre Barbéris, AREVA NP:—You use Pourbaix diagrams (thermodynamic data) to explain the late oxidation of iron and nickel. However, you observed the same iron profile on different samples, which implies the same oxygen potential gradient and different profiles for nickel, which means different oxygen potential gradients. How do you fit both observations together? Was it an effect of microstructure (SPPs, etc.)?

Authors' Response:—Precipitate size and density were measured for these samples, but no clear relation between hydrogen pickup and precipitate density was seen. However, it was noticed that, in high-hydrogen pickup samples, small nickel-containing precipitates dissolved, whereas large precipitates grew. It was also noticed that, in high-hydrogen pickup samples, the nickel/iron ratio slightly increased compared with that of low-hydrogen pickup samples. We are not quite sure that the observation of similar iron profiles implies that the oxygen potentials are the same. It could be that small differences were hidden compared with the large differences in nickel. An interesting question is why there would be such a large difference in nickel oxidation between two Zircaloy-2 samples.

Question from Brent Heuser, University of Illinois at Urbana-Champaign:—How unique are fits to XANES spectra to derive metal fraction as a function depth?

Authors' Response:—In fitting the results, it is clear that the metal spectra are noticeably different from the oxide spectra, whereas there is great similarity among oxide spectra and among metal spectra. Thus, by grouping the fits as a sum of metal spectra versus a sum of oxide spectra, the results are quite consistent.